Materials Characterization 200 (2023) 112907

Contents lists available at ScienceDirect

Materials Characterization

journal homepage: www.elsevier.com/locate/matchar

An investigation on the fatigue behavior of additively manufactured laser shock peened AlSi7Mg alloy surfaces

Milad Hamidi Nasab [a,c,*], Maurizio Vedani [c], Roland E. Logé [a], Navid Sohrabi [a], Amir Mohammad Jamili [a], Anton du Plessis [b], Stefano Beretta [c]

[a] Thermomechanical Metallurgy Laboratory – PX Group Chair, Ecole Polytechnique Fédérale de Lausanne (EPFL), 2002 Neuchâtel, Switzerland
[b] Research Group 3DInnovation, Stellenbosch University, Stellenbosch 7602, South Africa
[c] Department of Mechanical Engineering, Politecnico di Milano, Italy

ARTICLE INFO

Keywords:
Additive manufacturing
Laser powder bed fusion
Laser shock peening
Residual stresses
Fatigue

ABSTRACT

In the recent years, laser powder bed fusion of aluminum alloys has attracted extensive attention due to their capacious application in the biomedical, aerospace, and other industrial sectors. This is due to the combined capabilities of the laser powder bed fusion process and aluminum alloys bringing about complex shapes with high performance associated with light-weight design. Despite their high potential, parts produced by laser powder bed fusion suffer from residual stresses, surface irregularities and sub-surface defects limiting their full exploitation in fatigue sensitive applications. Consequently, post-processing methods such as laser shock peening can be employed to countermeasure these short-comings. This article reports on the effect of laser shock peening on the fatigue life of AlSi7Mg alloy fabricated via laser powder bed fusion. Laser shock peening induced a substantial improvement (around 50%) in the fatigue life when compared to the as-built parts. The improvements were attributed to the closure of surface and sub-surface pores, re-entrant surface features and in particular, induced compressive residual stress profile. The effects of laser shock peening were investigated through systematic multi-scale analysis through destructive and non-destructive methods. Furthermore, a simple fracture mechanics model was utilized to elucidate the effect of induced compressive residual stresses as the principal actor in the corresponding fatigue life improvement.

1. Introduction

Laser Powder-Bed Fusion (L-PBF) is an Additive Manufacturing (AM) process that relies on a laser to selectively melt successive layers of metallic powder according to a given scanning strategy [1–3]. In the past two decades, L-PBF attracted much attention in industry and academia as a new fabrication method enabling the production of complex geometries with short lead time and low material wastage. Despite these advantages, the high surface roughness, the formation of defects such as porosity [4,5] and the presence of a high level of tensile residual stresses (TRS) [6] significantly impact the fatigue properties and impede a broad-range industrialization of L-PBF parts [5,7–13]. Various strategies have been developed in the past 10 years to address these issues, with most efforts being concentrated on post-process treatments of L-PBF parts [14]. These include on one hand volumetric treatments such as heat treatments for residual stress relief, or Hot Isostatic Pressing (HIP) for porosity reduction, and on the other hand surface treatments for roughness reduction [9,15,16].

The efficiency of HIP has been largely documented for the removal of gas pores, lack-of-fusion defects, and even large-scale internal porosity. However, Du Plessis and Macdonald [17] showed that HIP was not effective in removing all internal pores, with some pores shrinking beyond the detection limit, and re-opening upon subsequent heat treatment. Besides, HIP is incapable of closing sub-surface defects connected to the surface because of the presence of confining gas into the pores during the treatment [18]. Such pores located in near-surface regions are particularly detrimental to fatigue properties acting as “killer” defects during cyclic loading and contributing to the larger scatter in the fatigue life [19]. A previous work investigated the combined effect of surface features and volumetric defects on the fatigue properties of AlSi7Mg and demonstrated that deep cavities and sub-surface pores cause large stress intensities and favor fatigue crack nucleation [7].

Surface treatments such as machining, vibro-finishing or (electro-) chemical etching can remove critical surface features acting as notches

* Corresponding author at: Rue de la Maladière 71b, 2002 Neuchâtel, Switzerland.
E-mail address: Milad.hamidinasab@epfl.ch (M. Hamidi Nasab).

https://doi.org/10.1016/j.matchar.2023.112907
Received 4 November 2022; Received in revised form 20 January 2023; Accepted 7 April 2023
Available online 8 April 2023

and favoring local stress concentration and fatigue crack initiation [20]. In order to further enhance fatigue properties, the introduction of compressive residual stresses (CRS) in the near-surface region through specific surface treatments such as sand blasting [21], shot peening [22] or laser shock peening (LSP) [23–27] has demonstrated its efficiency. In sand blasting and shot peening, the surface of the part is impacted with a high-pressure stream of abrasive material or with shots of small metallic or ceramic balls, respectively, generating a layer of high compressive residual stresses via plastic deformation of the near-surface region [28,29]. In addition, shot peening favors pore closure in the sub-surface region [30]. Although it has been reported that shot peening was influential in the improvement of fatigue strength [29,30], increasing the surface roughness and cracking of subsurface precipitates in the soft materials could have a negative effect on the fatigue performance of the part [31].

Among the processes mentioned above, LSP is a well-established post-processing method to improve the fatigue performance of metallic parts in aerospace applications such as jet engines and compressor blades [23]. During LSP, high-intensity laser pulses generate a hot plasma whose expansion underneath a thin water layer creates a pressure wave that propagates into the material, compressing it to depths that can vary depending on the LSP process parameters [20,23,32,33] In industrial applications, e.g. in aeronautics, geometrical features such as small fillet radii, sharp edges and notched areas act as local stress concentrators upon cyclic loading. Unlike shot peening, LSP can be selectively applied to such localized potential fatigue failure “hot spots” in order to induce compressive stresses over small areas and enhance the fatigue life accordingly [20,23,34]. Furthermore, LSP applies a higher level of CRS with respect to shot peening, hence increasing the effective depth of the affected material [35].

Most of prior research works reported an increase in the fatigue life of various alloys after LSP compared to as-built (AB) L-PBF condition or even to wrought material [23,24,35,36]. This is attributed to the elimination of tensile residual stresses, which are often replaced by extensive CRS and to the microstructural changes (i.e. grain refinement and higher dislocation content [24,32,33,37–47] that LSP can induce in the surface and near-surface layers. Furthermore, LSP demonstrated its ability to close critical (sub-)surface pores [48] typically acting as crack initiation sites. Luo et al. reported a 23.6% increase in the fatigue strength of LSPed TC17 titanium alloy, compared to AB condition [24]. Hackel et al. observed that laser peening provides a fatigue strength improvement in the range of 60% for notched L-PBF 316 L specimens [23]. Yella et al. reported an improvement in fatigue life of 316LN LSP samples by about 12.5% [49]. Huang et al. measured an increment of 48–75% on fatigue life for LSPed TC4 titanium specimens depending on the applied laser power density [50], while according to Yang et al., fatigue life is increased by about 2.5 times in the High-Cycle Fatigue (HCF) regime after LSP of a Ti6Al4V titanium alloy [51].

However, contradicting reports were made by Qin et al. and Jiang et al. who observed a decrease in the fatigue life of LSP-treated specimens, for 2024-T351 aluminum alloy and Ti6Al4V alloy under high cycle and ultra-high cycle fatigue conditions, respectively [36,52]. With most of the crack initiation sites being located in the subsurface region of the specimens after LSP, Qin et al. attributed this decrease in HCF strength to the tensile residual stresses (TRS) induced in this region to balance surface compressive residual stresses, promoting fatigue crack initiation and growth through the increase of the effective mean stress during fatigue loading [52]. Jiang et al. made similar observations, highlighting fatigue cracks initiating from an internal defect in some laser-shock peened specimens. Additionally, they reported an increase in surface roughness related to LSP, which is detrimental to the final fatigue strength, especially in the UHCF regime [36].

The present paper aims at evaluating the effect of LSP on the fatigue properties of AlSi7Mg specimens manufactured by L-PBF, which, to our knowledge, has not yet been documented in the literature. Using different sets of L-PBF process parameters, three different types of surfaces with specific features (e.g. attached spatter particles, open surface cavities, overhangs, closed sub-surface pores) are tailored in order to evaluate the effect of such (sub-)surface artifacts on the LSP process efficiency, in terms of post-LSP surface morphology, microstructure, residual stress distribution, defect distribution and resulting fatigue behavior.

2. Materials and methods

2.1. Material and sample manufacturing

All samples in this study were manufactured by L-PBF utilizing a Renishaw AM250 system (Wotton-under-Edge, UK) that utilizes a single mode pulsed fibre laser with a maximum power of 200 W, focused to a spot size of 75 μm. The powder adopted was a commercial gas atomized AlSi7Mg (A357) alloy supplied by LPW Technology (LPW Technology Ltd., Runcorn, UK), whose chemical composition is reported in Table 1.

Cuboid specimens with a size of 15 mm × 15 mm × 10 mm were printed on the reduced volume build platform (RBV) in a circular distribution, with equal radial distance (50 mm) and orientation from the axis of the laser source to avoid the effects of position dependency on the printed parts. All samples were printed with identical core process parameters (defined according to previous experience) and different contour line process parameters in order to generate different surface features and promote various sub-surface defects, mainly located at the contour-core interface regions. The energy input of a single scan vector (e.g. contour line energy E_L) for a L-PBF system equipped with pulsed laser can be calculated by the ratio of the laser power (P_L), the exposure time (t_S) and the point distance (P_d) according to Eq. 1.

$$E_L = \frac{P_L.t_s}{P_d} \tag{1}$$

The process parameters of the core and contour line used for the manufacturing of the cubes are presented in Table 2 and Table 3 respectively, where T_L, D_h, and r_0 are the powder layer thickness, hatch distance, and spot size, respectively. If we consider the data about hatch distance and spot size given in Table 2, we can observe that a significant overlapping of the tracks is expected. A relatively large overlapping of the tracks (both laterally and in-depth) is desirable to improve the homogeneity of the structure and circumvent defects related to lack of fusion at track edges. A number of line energies were chosen based on results previously published by the authors [7] to deliberately tailor distinct surface features in pursuance of drawing a better outline on the effect of surface irregularities on the fatigue behavior of AlSi7Mg alloy obtained by L-PBF.

2.2. Laser shock peening (LSP)

Once the cubic specimens were manufactured via L-PBF, they were subjected to LSP in the as-built condition. LSP experiments were done utilizing a Nd:YAG SAGA HP laser source (Thales Group, France) operating at 1064 nm of wavelength with a pulse duration of 6.3 ns under water confinement regime. A laser spot of 1 mm with a laser energy of 1 J and a pulse frequency of 5 Hz was chosen, based on previous investigations on a wide range of metallic alloys [35,46,47]. This gave a power density of 18 GW/cm^2. Utilizing the empirical equation $P\ (GPa) = 1.75\sqrt{I_0}\ (GW/cm^2)$ from [53], the pressure created at the surface of the part was estimated at 7.4 GPa. The beam spatial energy distribution was set to top-hat with a near-Gaussian pulse shape. The LSP treatments

Table 1
Chemical composition of the AlSi7Mg alloy powder (wt%).

Si	Mg	Mn	Fe	Ti	Zn	Cu	Al
6.7–7.3	0.25–0.45	0.5–0.6	0.14	0.08–0.12	0.09	0.04	bal.

Table 2
Core process parameters used in the building of the AlSi7Mg samples.

P_L (W)	t_s (μs)	P_d (μm)	T_L(μm)	D_h(μm)	r_0 (μm)
200	140	80	25	100	75

Table 3
Contour line process parameters used in the building of the AlSi7Mg samples.

Surface code	P_L (W)	t_s (μs)	P_d (μm)	E_L (J/m)
S01	200	140	80	350
S05	150	42	50	125
S07	100	42	50	83

were applied to the side vertical surface of 9 cubic specimens (three specimens per surface code) with a spot overlap of 50% (all parts of the surface are scanned at least twice) to evaluate the distribution of the residual stresses with respect to the initial surface roughness profile.

2.3. Residual stress measurements

Hole Drilling Method (HDM) was employed for the residual stress measurements of the AB and LSPed surfaces, using a RESTAN – MTS 3000 (SINT Technology, Italy) hole drilling instrument. This technique is widely used for the determination of in-depth residual stress profiles in parts subjected to high energy impact-based surface treatments [54]. The measurements were done according to the ASTM standard E837 [55]. In this process, a 1.8 mm diameter hole with 1 mm depth is drilled into the specimen and the strain resulted from residual stress relaxation due to the drilling is obtained by a strain gage rosette with three grids. Residual stresses were measured on the surfaces of samples produced according to the three parameter sets (S01, S05 and S07), in AB and LSPed conditions, with three repetition per case (18 measurements in total). A variable depth increment was applied to achieve more precise results in the near surface region. In the region from the surface down to 100 μm depth, measurements were carried out every 10 μm; from 0.1 mm to 0.5 mm in depth, measurements were done every 25 μm; and from 0.5 mm to 1 mm, every 50 μm.

2.4. Microhardness measurements

Microhardness profiles in depth were collected using LSPed cross-sectioned samples, testing the evolution of microhardness when moving from the surface directly exposed to LSP process into the depth of the specimen. Vickers microhardness were done using a 10 g load and a 12 s hold time at room temperature, utilizing a Q10A instrument (Qness GmbH, Germany). The distance between two consecutive indentations followed the recommendation from ISO 6507-1. Three parallel rows per specimen (S01, S05 and S07) of 30 indentation separated by 50 μm gapes were made along the specimen's depth. The average microhardness and the corresponding standard deviation were plotted by considering three measurements at each depth level per specimen.

2.5. Morphology, metrology and texture analysis of the surfaces

A non-contact-based metrology method was employed to distinguish the effect of LSP on the morphological aspects of the L-PBFed AB surfaces. These measurements were obtained by employing a Keyence VK-X1100 confocal microscope equipped with violet semi-conductor laser with lateral resolution of 1 nm and a vertical resolution of 0.5 nm. The specimens were measured utilizing a 10 × 0.3 NA (numerical aperture) objective and an areal test field of 2.9 mm × 2.9 mm. Nine acquisitions, each 1 mm × 1 mm in size, were collected for each sample and stitched together with 5% overlapping. Before any surface parameter calculation, the three-axes raw data were subjected to a linear form removal, followed by a spatial filter (median denoising 5 × 5) to remove spurious points. Subsequently, a Gaussian convolution F-filter with a 2.9 mm cut-off was applied equal to the length of the test field in order to eliminate the waviness at scales larger than the field of view, thus obtaining S—F surfaces. Afterwards, another Gaussian convolution L-filter with a 0.8 mm cut-off was applied to circumvent smaller scale waviness, thus obtaining S-L surfaces. These cut-off values were selected based on visual inspection of the analysed surfaces and in agreement with previously published works [56]. The data were then processed to obtain the surface parameters based on the ISO 25178-2 starndard [57].

Images of the surface profile were obtained from the samples sectioned along planes parallel to the build direction (z axis) after grinding, polishing and etching by Keller's reagent. The images were taken employing a Nikon Eclipse LV150NL optical microscope (OM) to acquire a detailed evaluation of the sub-surface defects. Particular attention was paid to the microstructure along the regions intersecting the surface profiles and just beneath them, in the altered material zone [58]. Furthermore, Surface morphology and microstructural analysis were done using a Zeiss-Gemini2 field emission scanning electron microscope (SEM). SEM-EDX analysis were done on the LSPed surfaces to investigate the possible surface contamination as a result of the LSP process. Electron Back Scattered Diffraction (EBSD) maps were acquired close to surfaces of fatigue specimens sectioned along the build direction with the same microscope equipped with the Symmetry camera and Aztec acquisition software (Oxford instruments). The maps were acquired at 25 kV with the step size of 0.5 μm with the acquisition rate of 200 Hz with detection of 10 bands, gain of 2 in mode speed 1.

2.6. Fatigue testing

The three sets of represented surfaces (S01, S05 and S07) were selected to evaluate the potential improvement in fatigue performance induced by LSP with respect to the AB surfaces, already investigated and published by current authors [7].

Ten three-point bending fatigue samples per surface condition were thus fabricated using the process parameters for the core and contour scans presented in Table 2 and Table 3 respectively, according to the design depicted in Fig. 1a. The fatigue specimens were printed horizontally with the surface of interest being parallel to the build direction (Fig. 1b). In order to accelerate the tests and reduce the experimental efforts for evaluating the effects of LSP on the AB surfaces and the corresponding fatigue properties, the design proposed by Boniotti et al. [59] was employed for these small specimens. Prior to the LSP treatment, the fatigue specimens were subjected to direct aging at 160 °C for 4 h (T5 heat treatment) [60]. Consequently, the specimens went through LSP treatment with the parameters presented in Section 2.2. The LSP treatment was applied to the central area of the fatigue specimens' curve with a treatment length of 12 mm Fig. 1c and e.

Three-point bending fatigue tests were performed in the load-controlled mode utilizing an MTS Acuman 3 electrodynamic test system equipped with a load cell with maximum capacity of 3 kN. The fatigue tests were performed on the LSPed samples with a load ratio R of 0.1 in an ambient temperature environment, at constant stress ranges, with a maximum applied stress varying from 200 to 300 MPa, to investigate fatigue lives ranging from 4×10^4 cycles to the runout limit, which was set to 5×10^6 cycles under frequency of 30 Hz. Finally, Post-mortem fractographical analyses were performed on all the broken fatigue specimens utilizing the SEM to identify on fracture surfaces the nucleation site, the extent of crack growth region and to perform statistical analysis on their extents.

2.7. X-ray tomography investigation

To measure the porosity in the AB and LSPed fatigue specimens, X-ray tomography was applied via typical laboratory micro-CT equipment at the Stellenbosch CT facility [61]. Two fatigue samples per category

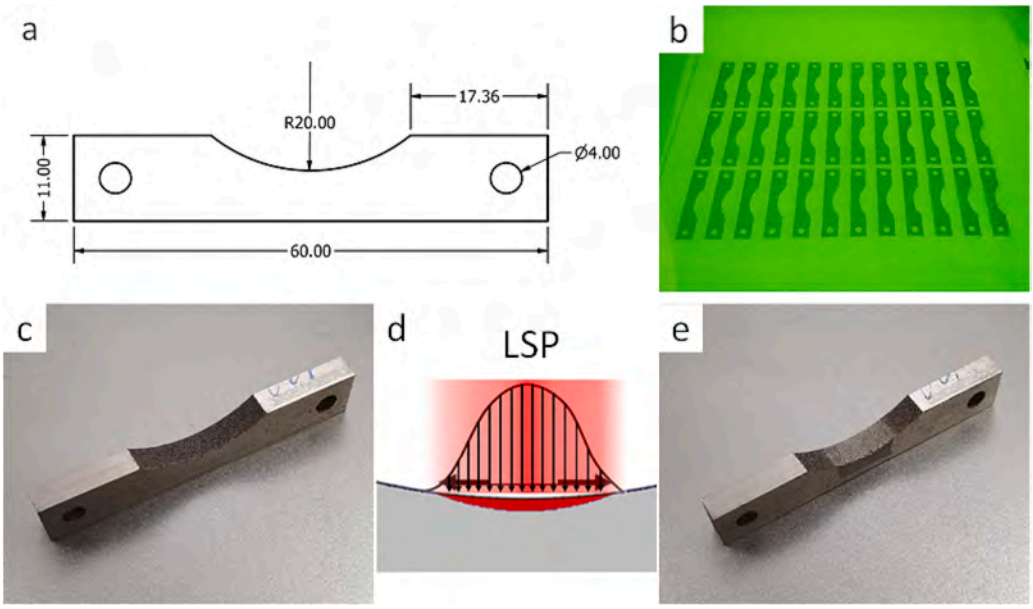

Fig. 1. (a) Geometry of the three-point bending fatigue specimens printed via L-PBF using AlSi7Mg powders; (b) printing orientation with the surface of interest being parallel to the build direction; (c and e) AB and LSPed fatigue specimens, respectively; (d) schematic of the LSP profile onto the surface of the specimens.

(S01, S05 and S07) and condition (AB and LSPed) were tested by non-destructive X-ray tomography prior to the fatigue tests.

The voxel size of the micro-CT scan was selected as 15 μm, allowing analysis of all pores and surface features larger than this value, and providing a field of view enveloping most of the sample's critical surface and sub-surface volume. Scan parameters included 150 kV and 100 μA for X-ray generation, with 0.5 mm copper beam filter. The sample was loaded in the micro-CT equipment with its longer axis vertically and rotated around this axis during the scan. A full 360-degree rotation was used for scanning in 2000 steps, at each step position the first image was discarded and the subsequent 3 images were averaged. Detector shift was enabled to minimize ring artifacts [12].

3. Results

3.1. Morphology of the surfaces

The representative SEM images of the three AB and LSPed surfaces are presented in Fig. 2 and Fig. 3 respectively. The most notable features exhibited on the AB vertical surfaces are the presence of partially fused spatters and melted powder particles both showing a wide variability in their size. The three different AB surfaces demonstrated diverse features in terms of type, size and amount of the above features. A substantially dense surface was observed in case of S01 specimen with presence of large spatters (showed with green arrows in Fig. 2) and partially melted metal powder particles stuck onto its surface (showed with dotted blue rectangle in Fig. 2). In samples deposited with lower contour line energies (S05 and S07 samples), formation of cavities on surfaces was observed (showed with red arrows in Fig. 2b and 2c) as a result of insufficient applied energy density, incapable of fully melting the attached spatters and leaving behind cavities around the spatters. Furthermore, S07 surface showed higher number of attached particles on the surface which might be due to balling phenomena owing to Plateau-Rayleigh instabilities triggered by low deposited energy and the corresponding high scanning velocities.

Upon application of LSP on the AB surfaces, the observed features in Fig. 2 were substantially eliminated due to the impactful waves delivered via LSP, resulting in removal or deformation of the above-mentioned features. LSP treatment resulted in the removal of partially fused spatters and metal powders, improving the flatness in S01 surface (Fig. 3a) while it only accompanied the removal of fused features in S05 and S07 surfaces (Fig. 3b and 3c). Instead the LSP treatment arose higher cavity density in both surfaces, which could be attributed to the already existing sub-surface porosities which surfaced after the subsequent LSP treatment.

Taking a closer look at the magnified LSPed surfaces (Fig. 3d and 3e), a lay in the surface texture is seen which could be an indication on the plastic deformation during the LSP process. EDS analysis of the LSPed

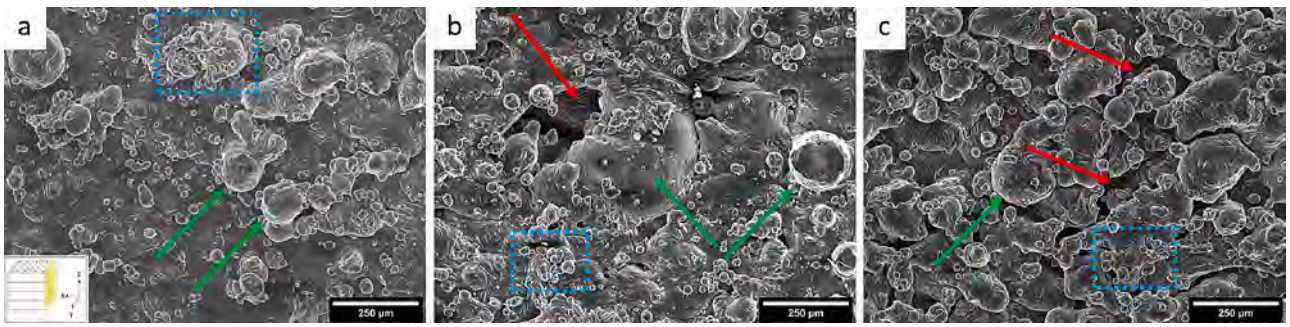

Fig. 2. SEM images of the lateral AB surfaces (parallel to the build direction) of the cubes printed under different contour applied energy by L-PBF: (a) S01 $E_L = 350$ J/m; (b) S05 $E_L = 125$ J/m; (c) S07 $E_L = 83$ J/m. The images show the presence of large spatters (green arrows), partially melted metal powder particles (dotted blue rectangle) and cavities (red arrows) attached to the surface.

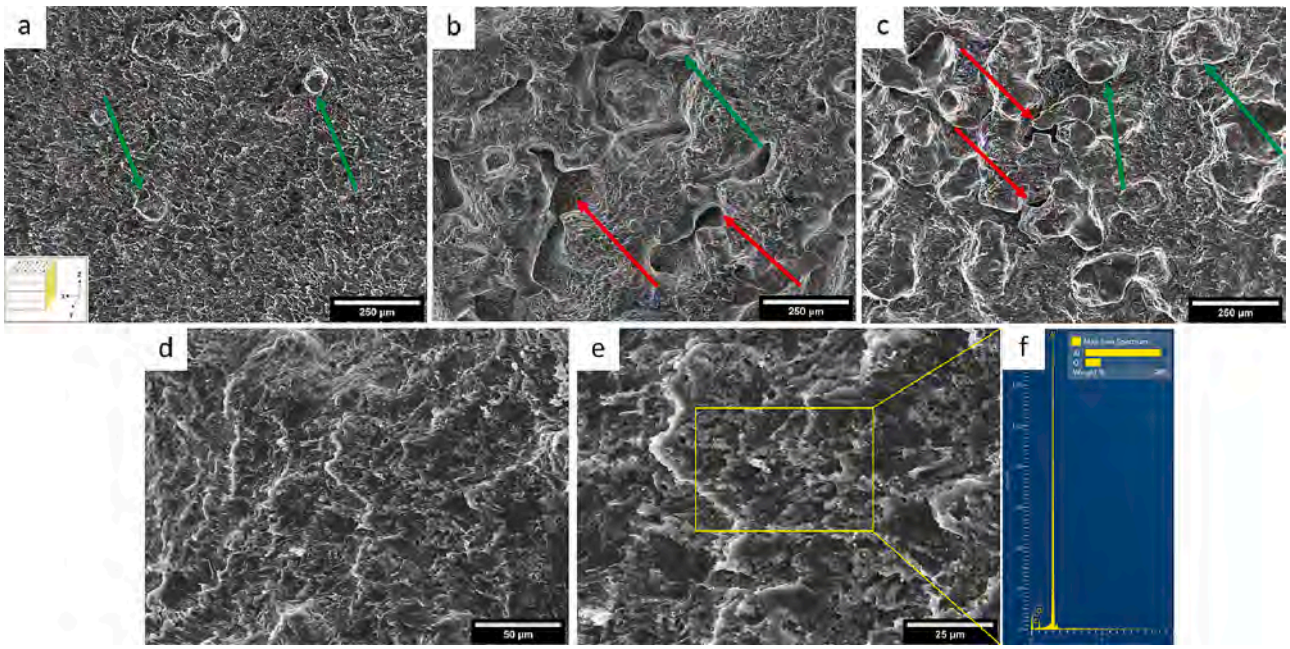

Fig. 3. SEM images of the lateral LSPed surfaces (parallel to the build direction) of (a) S01, (b) S05 and (c) S07; (d) high magnification of the LSPed S01 surface; (d and e) areal EDS of the LSPed S01 surface. The images show the remaining of large spatters (green arrows) and cavities (red arrows) on the surface after LSP treatment.

surface recorded a thin layer of aluminum oxide on the surface; which could be attributed to the type of confinement used during the LSP treatment (water) and the plasma induced via laser-material interaction and subsequent formation of aluminum oxide on the surface.

3.2. Topography of the surfaces

Surface topographies of AB and LSPed surfaces alongside their corresponding surface parameters is presented in Fig. 4 and Fig. 5, respectively. According to data presented in Fig. 4, the LSPed surfaces generally show a narrower height distribution. The S01 surface features a distribution skewed towards positive values indicating a surface dominated by peaks rather than valleys. After the LSP treatment, this skewness reduced in association with partial removal of peaks. On the contrary, LSPed S05 and S07 surfaces feature significant valleys with a shift towards negative values (valleys) in the height distribution graphs. This observation is supported by SEM images represented in Fig. 2 and Fig. 3.

Typical areal surface parameters based on ISO 25178-2 [57] were calculated based on data collected via confocal microscopy measurements. Three surface parameters were selected and evaluated based on their applicability on assessing the prospect effect of LSP process on the AB surfaces: the arithmetical mean height of the S-L surface (*Sa*), maximum valley depth (*Sv*) and developed interfacial area ratio (*Sdr*).

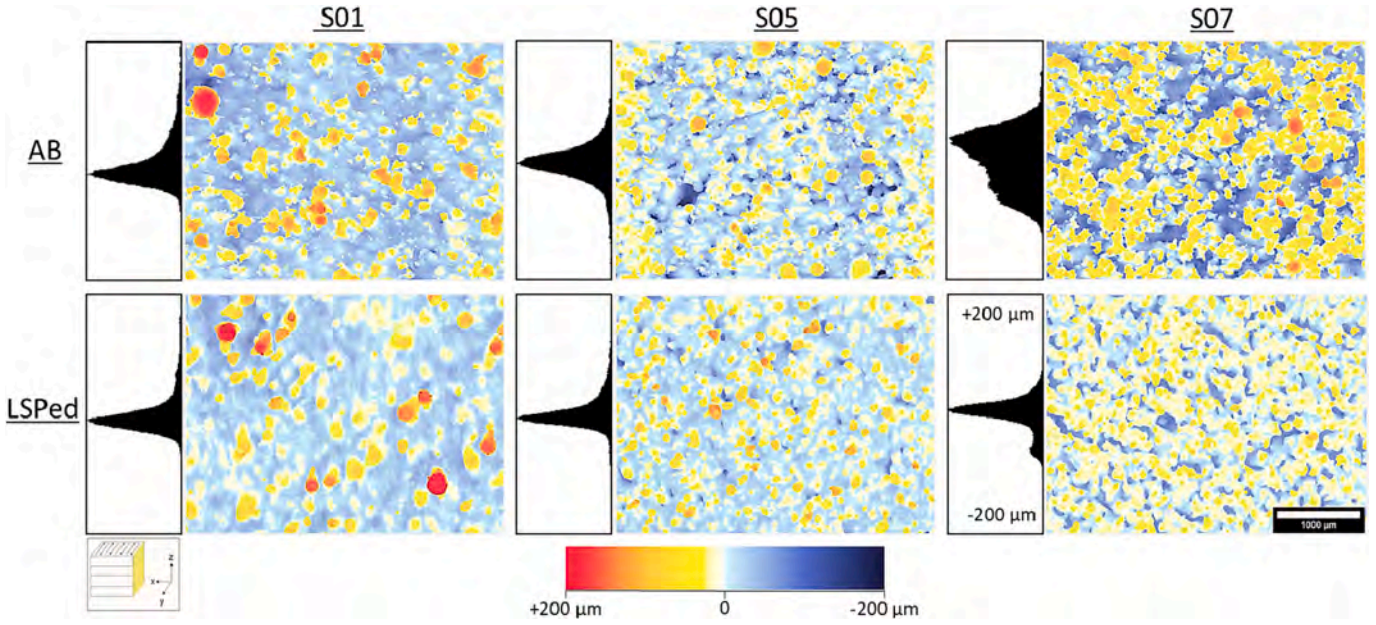

Fig. 4. Lateral surface topographies recorded via confocal microscopy; AB surfaces (top row) and LSPed surfaces (bottom row) of S01, S05 and S07 specimens. Height distribution for each surface is presented on its left side with a normalized frequency value for all surfaces. The image scaling is identical for all the surfaces.

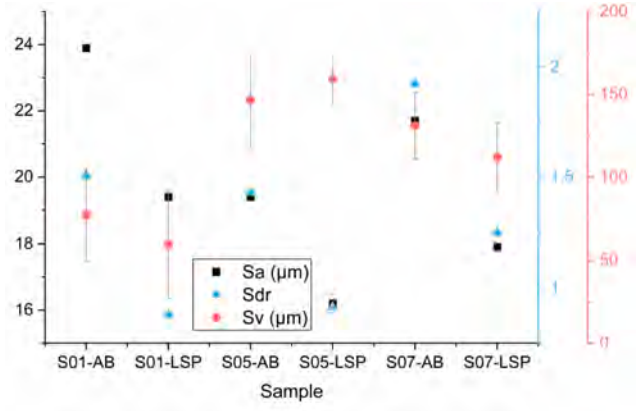

Fig. 5. Surface parameters: (a) Arithmetical mean height Sa, (b) Maximum valley depth Sv and (c) Developed interfacial area ratio Sdr measured by confocal microscopy.

Among these parameters, *Sv* is known to represent the deepest notch found on the surface, which has been shown to correlate with the fatigue life [7,21]. Therefore, the scanned area was divided into nine control areas and the Sv was extracted from these smaller areas to improve its statistical representation of the surface. These measurements were done on three specimens per category. Furthermore, *Sdr* represents the specific build up surface area due to the presence of surface anomalies compared to the perfectly flat area ($Sdr = 0$). It is worth to mention that conventional areal surface topography measurement methods such as optical focus variation or confocal microscopy have a limited ability to measure internal or re-entrant surfaces such as overhangs and undercuts, and they can be considered as "line of sight" techniques. Accordingly, the surface data produced by such techniques is generally created as a height map with a single z value corresponding to a specific (x, y) position. Therefore, surfaces between steps are interpolated, leaving behind surface *curtains* at re-entrant features [62]. Nonetheless, LSPed surfaces showed smaller Sdr values suggesting their evolution towards flatness via the subsequent plastic deformation of the AB surface peaks.

According to Fig. 5 and in agreement with qualitative evaluations resulting from confocal microscope images, a modest improvement is observed after the LSP process for all the AB surfaces almost with an identical trend. Based on these parameters, AB surfaces after LSP show a more similar characteristics compared to their own counterparts in AB condition. Statistical measurements show that the distribution of deepest surface features does not significantly change after LSP.

3.3. Microstructure and surface profile analysis

The sample surface profiles were investigated by microstructural observations of polished sections cut perpendicularly to the build direction to achieve a wider overview of the surface and in particular, sub-surface features created by L-PBF and the prospect effect of LSP process on these features. As expected, based on the results of topographical examination, the three AB surfaces exhibit diverse surface profiles in terms of continuity, surface and sub-surface features and the corresponding frequency of their occurrence. Moreover, *Re*-entrant features such as overhangs and undercuts became clearly visible from these surface profile images. S01-AB surface showed a solid surface with occasional presence of relatively large spatters and metal powder particles, which were mostly eliminated after the LSP process (Fig. 6a and b). S05-AB and S07-AB displayed a significantly higher number of re-entrant features and a more pronounced sub-surface porosity in S07-AB specimens. However, it is very clear that the LSP process was capable of closing a large number of these features in regions very close to the surface (Fig. 6c and e).

Fig. 7a and b provide closer views of the re-entrant features in AB surfaces. These defects are marked by red arrows. Moreover, the closure effect imposed by LSP process is demonstrated in Fig. 7c-e. From extensive analysis of cross-sectional profiles, it was found that the region plastically affected by the LSP process has a depth of around 50 μ*m* from the free surface. The shockwave induced by LSP penetrates the surface and creates multiaxial compressive forces, regardless of its impact direction [48]. The imposed compressive stresses can locally overcome the yield strength of the material surrounding the pores in these regions and cause plastic deformation driven pore closure (see Fig. 7e).

The grain structure of the AB and LSPed specimens are shown in the EBSD images reported in Fig. 8, with an examined surface area of 700 × 300 μm^2. The non-indexed points due to porosities are shown in black. The grain structure in AB specimens is fully columnar with narrow

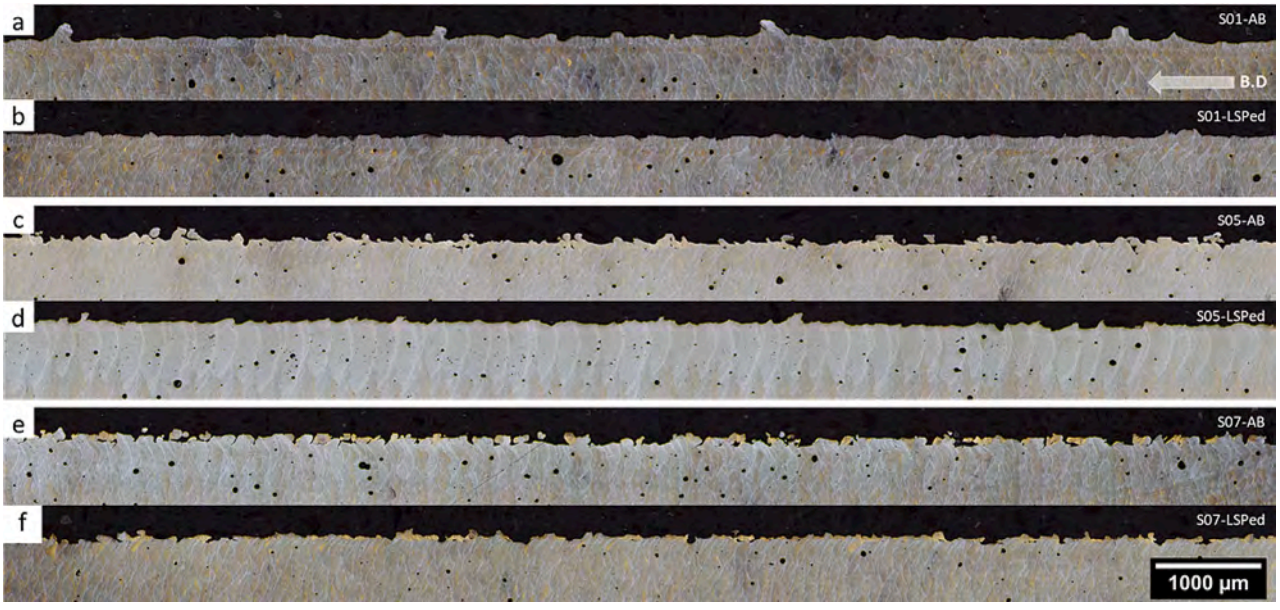

Fig. 6. Transverse sections of specimens taken close to surfaces by the OM: (a and b) S01 AB and LSPed surfaces; (c and d) S05 AB and LSPed surfaces; (e and f) S07 AB and LSPed surfaces. The profile length is 12 mm and the build direction is along the horizontal axis of the images (see white arrow on Fig. 6a).

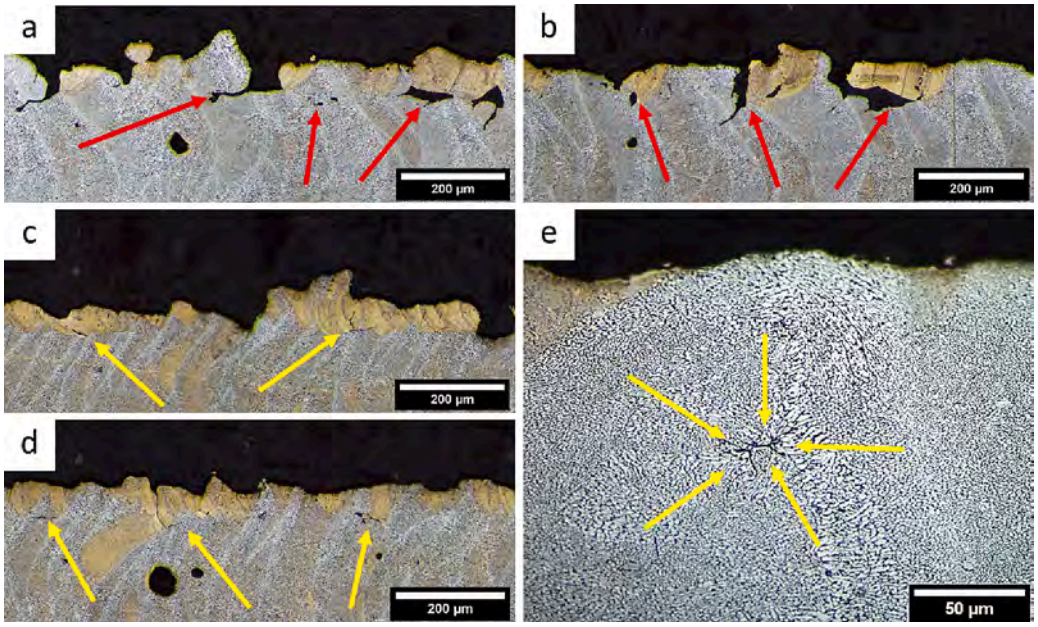

Fig. 7. Transverse views of S07 AB and LSPed cuboid specimen taken by; (a and b) open surface notches and closed sub-surface pores in AB surfaces (these features are shown by red arrows); (c and d) closure to surface notches and sub-surface pores after LSP process; (e) high magnification image of closed sub-surface pore after LSP process (these features are shown by yellow arrows). (For interpretation of the references to colour in this figure legend, the reader is referred to the web version of this article.)

grains elongated in the build direction. A similar grain structure is observed for the LSPed specimens. However, in the regions very close to the surface (down to 40 um below the surface), change in grain shape became evident as a result of LSP. The average grain aspect ratio in the vicinity of the surface (an area of 700 × 40 μm^2) was calculated via AztecCrystal (Oxford Instruments) using the fitted ellipse method. The average grain aspect ratio of 6.9, 5.8 and 6.5 for S01, S05 and S07 specimens in AB condition were measured. However, after the LSP treatment, the average grain aspect ratio of 6.1, 4.4 and 4.8 were reported respectively resulting in 13% - 26% decrease in its value.

3.4. Microhardness measurements

Fig. 9 presents the microhardness profiles for all sets of surfaces from the depth of 50 μm to 1.5 mm inside the bulk of the specimen. Plastic deformation induced strain-hardening as a result of the LSP process slightly increased the hardness (around 10%) in the region close to the surface to a maximum depth of 300 μm. The effect of strain-hardening was lower in S07 surface due to its hollow sub-surface structures and its compliance effect. In this case, a significant portion of the energy from each pulse is spent to deform and close the cavities close to the surface.

3.5. Residual stress measurements via hole drilling

Fig. 10 displays the evolution of the residual stresses throughout the 1 mm thickness layer from free surface of AB and LSPed samples. As expected, AB surfaces exhibit tensile residual stresses which is inherent to the L-PBF as a result of solidification of the molten material and the corresponding shrinkage effect. S05 and S07 specimens exhibited a very similar residual stress values at regions very close to the surface, where S01 specimen showed significantly lower residual stress values. The significant difference in the compressive residual stress values of AB S07 very close to the surface is due to the presence of excessive break points on the contour, incorporating into its relaxation during the solidification process. It is also well established that higher scanning speeds (S05 and S07) can result in higher cooling rates and less uniform shrinkage in the consolidated part [63]. Upon application of LSP and imposed stress waves from surface towards the bulk of samples, the compressive residual stresses take over, having their maximum value on the surface region and decreasing throughout the thickness down to a point when they shift from compressive to tensile regime. S01-LSPed specimen showed the highest value for the compressive residual stress compared to LSPed S05 and S07 initially. This could be attributed to the lower number of voids and cavities detected on surfaces of S01 specimens which would result in the absorbance and transmittance of a larger portion of the LSP energy compared to surfaces with porous, low density near surface regions (S05 and S07). It is also suggested that the porous regions might act as a damper layer, addressing the absorbed energy for pore closure and resulting in a more relaxed near surface region after the LSP treatment.

3.6. X-ray micro-computed tomography

Representative micro-CT snapshots from the lateral plane of the curved region in fatigue specimens in AB and LSPed conditions are illustrated in Fig. 11. The sub-surface region is magnified to better represent the contained surface notches and sub-surface porosities in AB condition and the corresponding improvement after the LSP treatment. It is confirmed that LSP was able to eliminate a large number of sub-surface pores in all the three conditions. However, this effect was more pronounced in S05 and S07 surfaces due to the higher presence of sub-surface porosities in AB condition. Moreover, the regions further away from the surface were not affected by the LSP induced plastic deformation. Furthermore, some of the deeper surface notches remained present after the LSP treatment, which is in-line with confocal microscopy surface measurements of the cubic specimens.

3.7. Fatigue test results

The results of the three-point bending fatigue tests of AB [7] and LSPed specimens are illustrated in Fig. 12. The tests proved to be repeatable and exhibited a limited scattering effect. AB fatigue results from the previous study [7] showed only a slight difference among the three surfaces, despite their significantly different characteristics. As expected, LSP fatigue results demonstrated the same trend between the surfaces with variabilities higher at lower stress levels which could indicate the proximity to the fatigue limit. An improvement in the range of 50–80 MPa was observed in the fatigue limit of LSPed specimens which correlates well with the changes in the residual stresses measured on the cubic specimens by hole drilling.

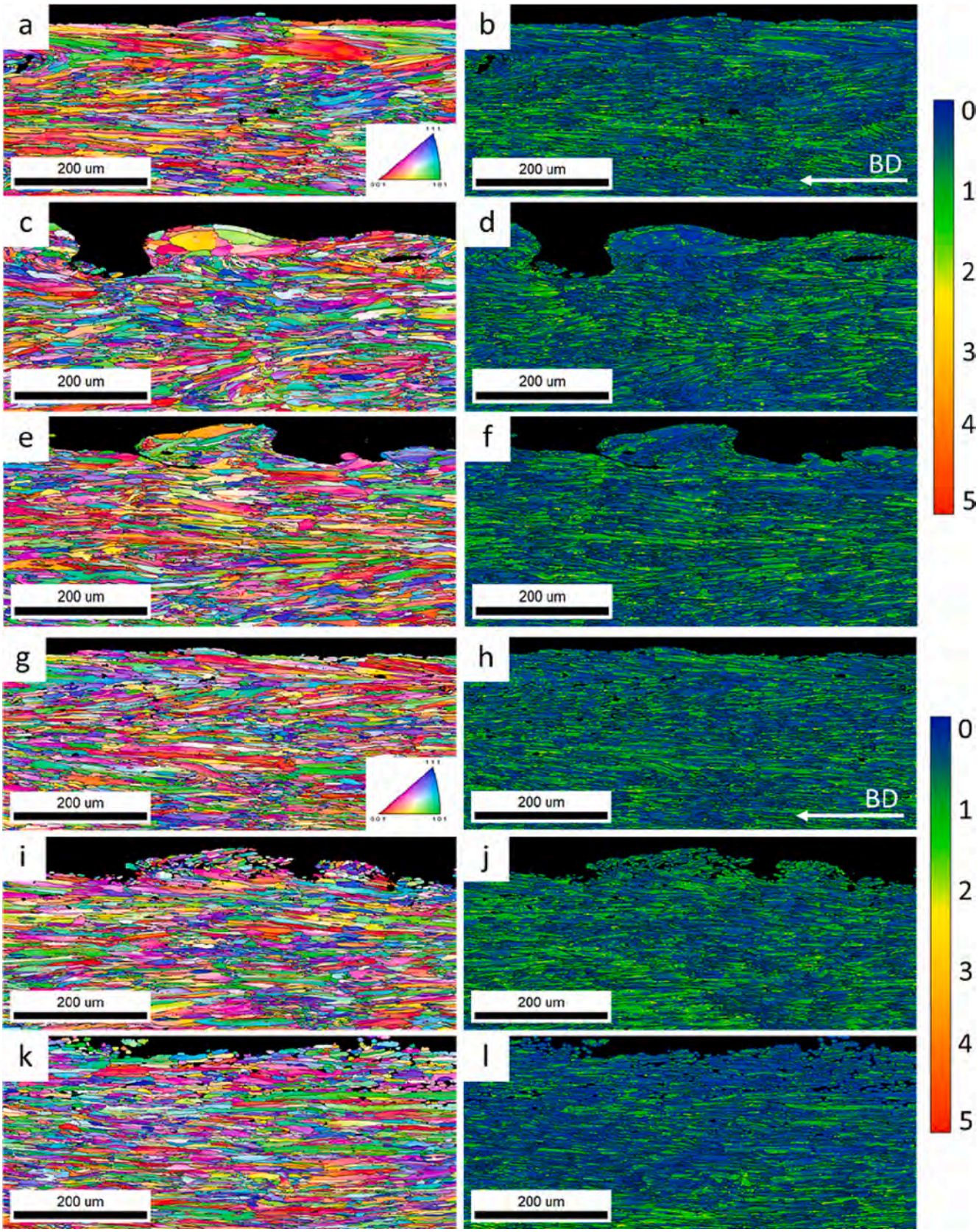

Fig. 8. EBSD inverse pole figures and Kernel average misorientation maps (KAM) of: (a & b) S01-AB; (c & d) S05-AB; (e & f) S07-AB; (g & h) S01-LSPed; (I & j) S05-LSPed and (k & l) S07-LSPed.

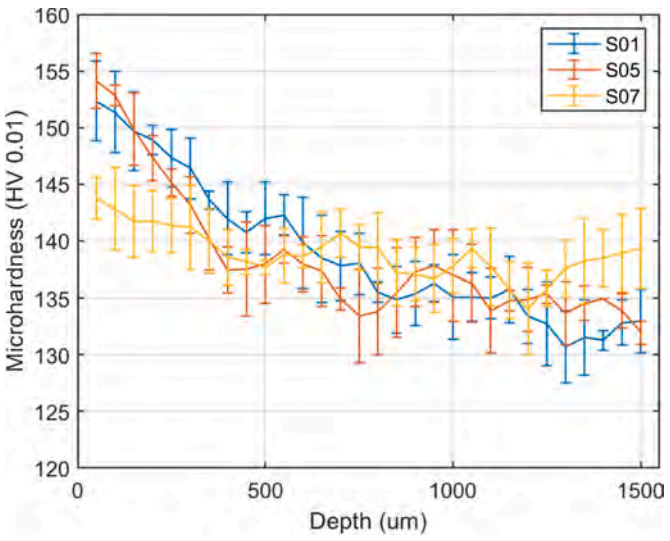

Fig. 9. Microhardness profiles along the depth of the specimen for the three S01, S05 and S07 surfaces.

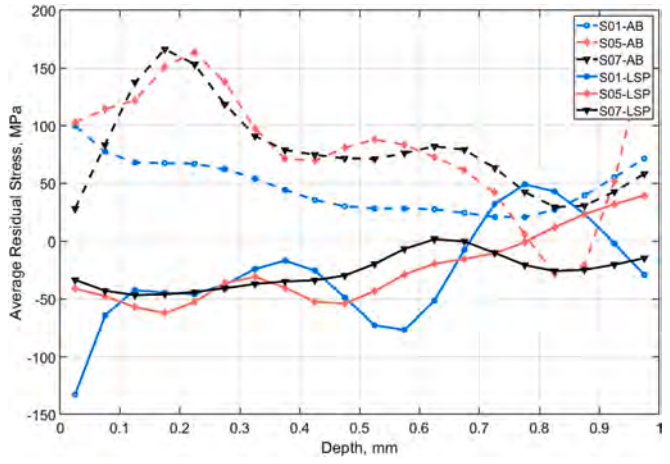

Fig. 10. Average residual stress values measured via hole drilling for AB surfaces (dashed lines) and LSPed surfaces (solid lines).

3.8. Fractography

Based on the post-mortem analyses performed in the previous study on the AB specimens for S01, S05 and S07 surfaces [7], all of the failures occurred from surface roughness or volumetric defects falling in the surface regions. After careful analysis of the LSPed failed fracture surfaces, a noticeable increase in surface induced failures was conveyed (see Table 4). The failure tendency towards surface defects might be the result of LSP's ability to close the sub-surface cavities, exposing the surface notches as viable failure initiation sites. S01 LSPed specimens (see Fig. 13) failed from surface defects with 67% of occurrence while no failure occurred in S01-AB specimens from the surface. S05 LSPed surfaces (see Fig. 14) exhibited a 43% occurrence of failure via surface defects; a trend similar to the AB counterparts. Moreover, S05 LSPed specimens usually failed through multiple crack nucleation at surface in higher stress ranges. Lastly, S07 LSPed (see Fig. 15) showed an occasional failure from bulk defects but they mostly failed through defects originated from the surface regions.

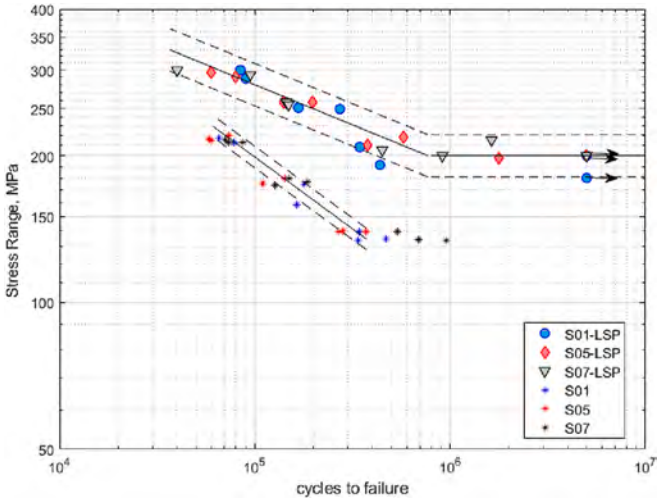

Fig. 12. Results of high cycle fatigue tests for AB surfaces (star marks) [7] and LSPed surfaces (filled markers on top).

Table 4
Fraction of failures due to surface defects in AB and LSPed fatigue specimens.

Surface code	As-built (declared from previous work [7])	LSP
S01	0%	67%
S05	44–55%	43%
S07	67–78%	90%

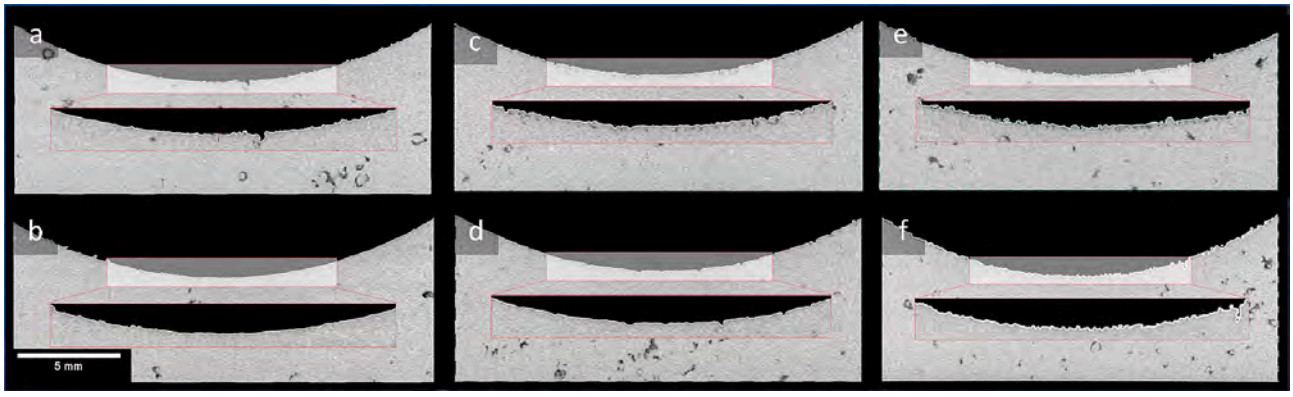

Fig. 11. micro-CT lateral plane snapshots of fatigue specimens and the corresponding magnified arc images. AB surfaces (above row) and LSPed surfaces (below row) of S01 (a and d), S05 (c and d) and S07 (e and f) specimens.

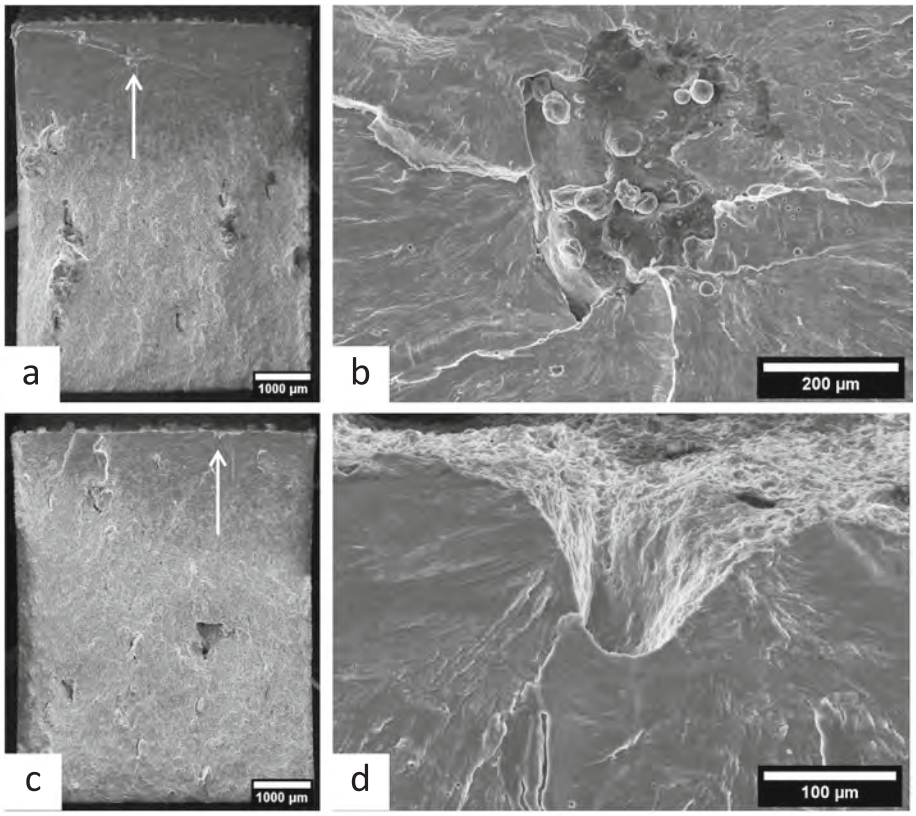

Fig. 13. SEM views of the fracture surfaces of two S01-LSPed specimens that failed due to bulk and surface defects: sample tested at stress range of (a and b) 220 MPa via bulk defect and (c and d) 300 MPa failed via surface defect. The white arrows indicate the fracture initiation sites.

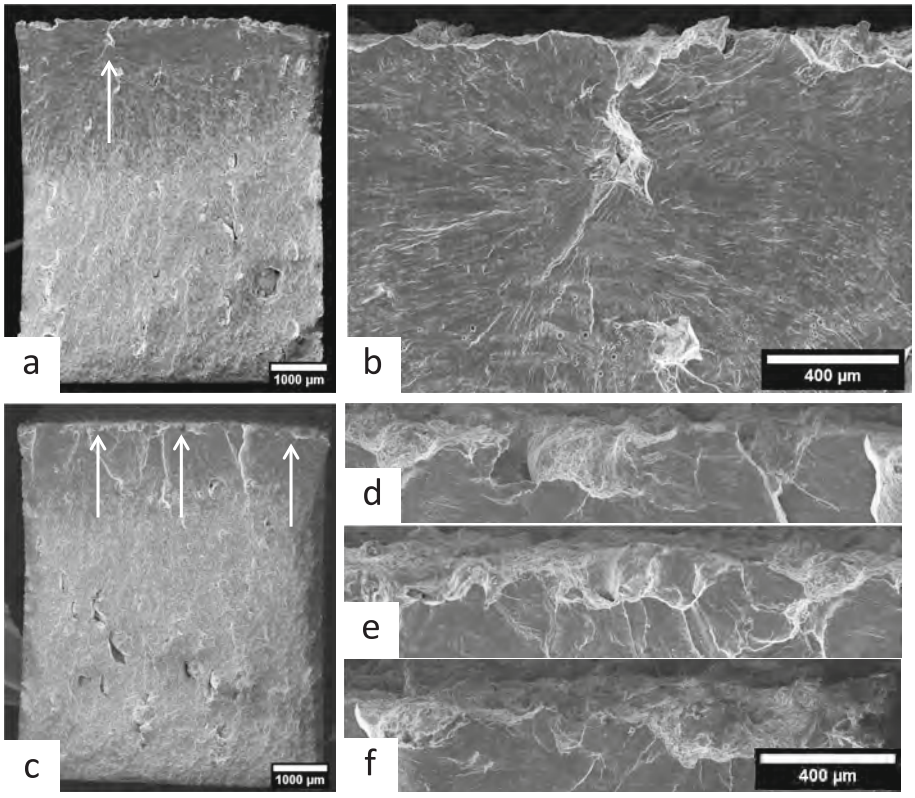

Fig. 14. SEM views of the fracture surfaces of two S05-LSPed specimens that failed due to bulk and surface defects: sample tested at stress range of (a and b) 220 MPa failed via a single initiation site and (c and d) 300 MPa failed via multiple initiation sites at surface. The white arrows indicate the fracture initiation sites.

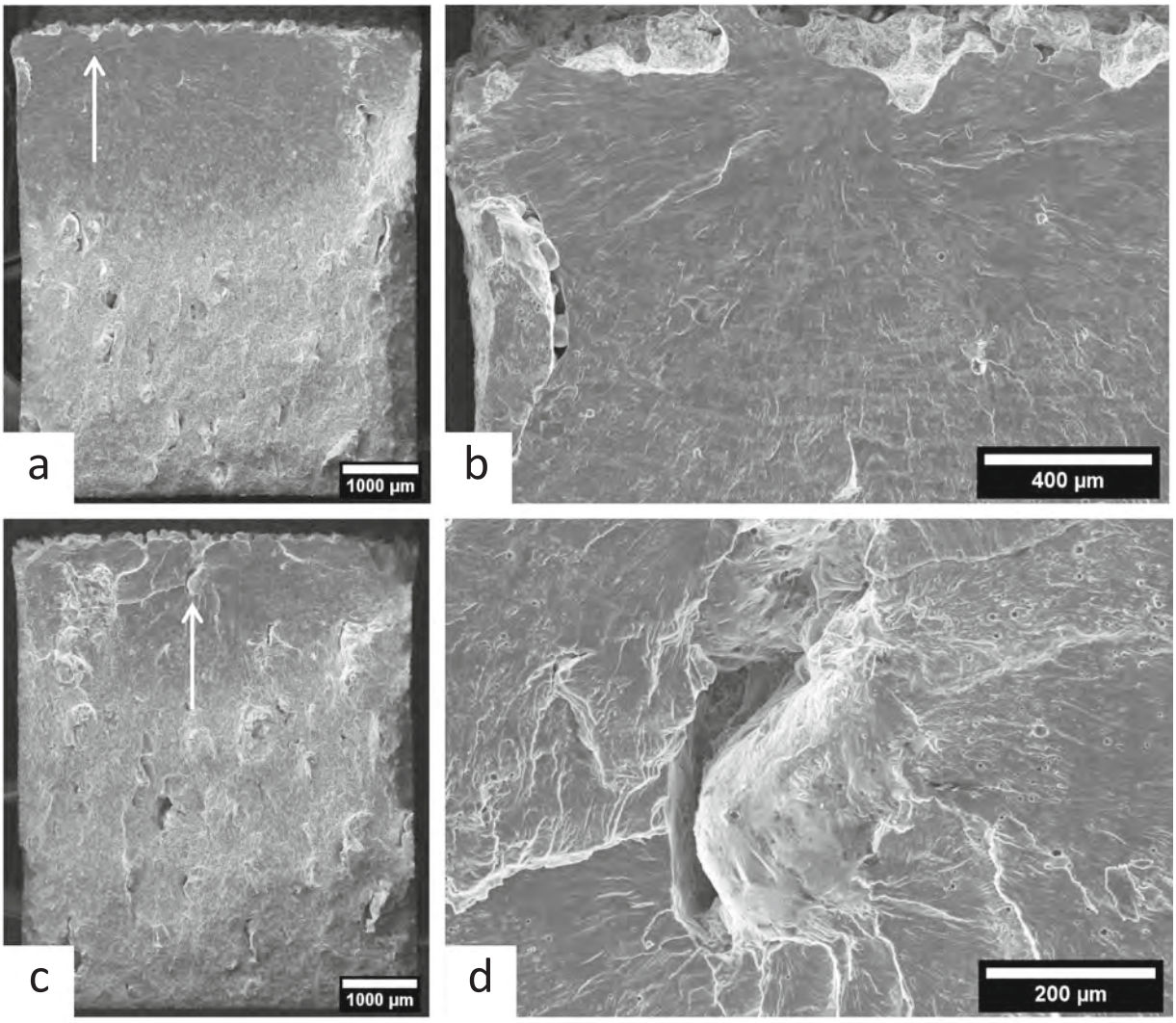

Fig. 15. SEM views of the fracture surfaces of two S07-LSPed specimens that failed due to surface and bulk defects: sample tested at stress range of (a and b) 220 MPa failed via surface defect and (c and d) 300 MPa failed via bulk defect. The white arrows indicate the fracture initiation sites.

4. Analysis of the fatigue test results

A comprehensive analysis of the fatigue data of the LSP specimens would be out of the scope of the present research work since a large number of different factors can potentially play a role on fatigue performance. First, there is a significant shielding effect on the surface due

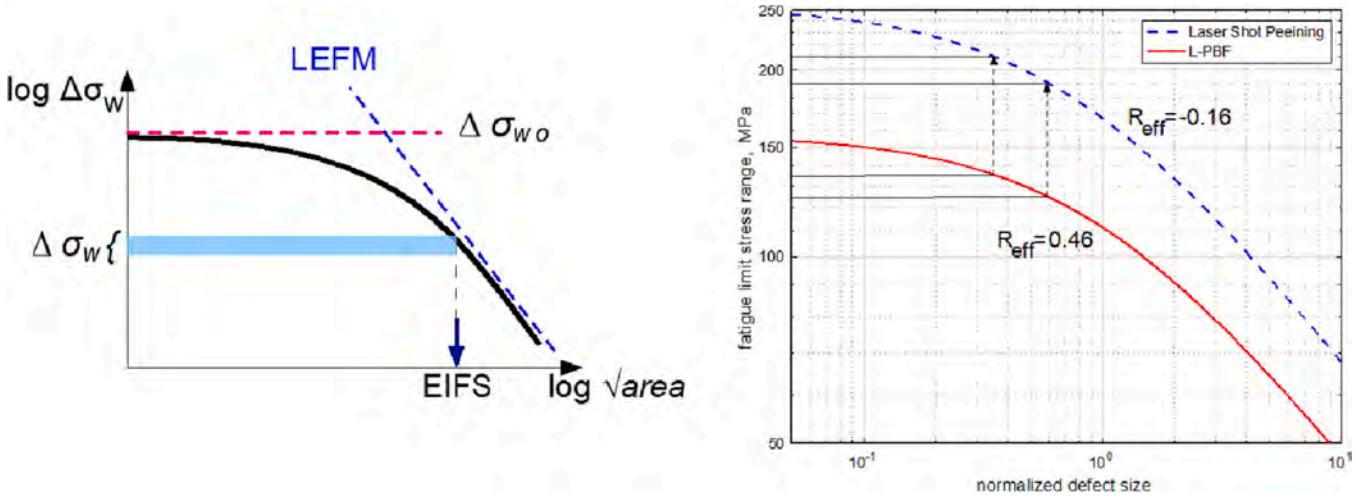

Fig. 16. The model for fatigue strength: (a) EIFS scheme; (b) estimation of the fatigue limit from AB to LSP specimens.

to the presence of many surface features [7]: a detailed analysis would require to have a CT scan of the specimens before and after fatigue tests [10] for every specimen to precisely identify the failure location based on reconstruction of the profile from the CT scan data. Second, the shape of the features of the fracture origin is ranging from deep defects (see Fig. 13b) to elongated shallow features (see Fig. 14d-e) to pit-like features (see Fig. 13d).

Therefore, considering that the LSP has not significantly changed the surface features (see Fig. 5), we decided to adopt an Equivalent Initial Flaw Size (EIFS) model [13,64], as depicted in Fig. 16a, where an equivalent defect size is calculated from the experimentally determined fatigue limit.

It has been clearly shown in the literature that surface features can be treated as short-cracks and that, among different models [9], a simple yet precise description of the fatigue strength can be obtained with a simple threshold model combining El-Haddad model [65] with Murakami's model for Stress Intensity Factor (SIF) [66]. In detail, the fatigue limit could be expressed as [13]:

$$\Delta\sigma_{\omega} = \Delta\sigma_{\omega o} \cdot \sqrt{\frac{\sqrt{area_o}}{\sqrt{area} + \sqrt{area_o}}} \tag{2}$$

where:

$$\sqrt{area_o} = \frac{1}{\pi}\left(\frac{\Delta K_{th}}{F.\Delta\sigma_{\omega o}}\right)^2 \tag{3}$$

The El-Haddad parameter is expressed in terms of $\sqrt{area}$ and F = 0.65 for surface defects [67]. The two material parameters in Eq.2 are ΔK_{th} and ΔS_{wo}, being the long crack threshold and the fatigue limit for smooth specimens, respectively [68]. The key point in applying these concepts is to correctly consider the effective stress ratio due to the presence of residual stresses [11,46].

Considering the presence of residual stresses, AB and LSP samples exhibited residual stress (σ_{res}) values of +100 MPa and − 50 MPa respectively in the first 100 μm below the surface. The effective stress ratio (R_{eff}) can be computed considering the fatigue limit experimentally obtained and the value of residual stresses close to the surface. R_{eff} for AB and LSP specimens is presented in Table 5.

Then applying the fatigue strength model and referring to material parameters obtained for AlSi10Mg [13] (fatigue test results on AlSi7Mg are quite close to AlSi10Mg), the prospective fatigue limit at different stress ratios is shown in Fig. 16b, where the defect size has been normalized with respect to $\sqrt{area}$. From the fatigue limit $\Delta S_w = 130$ MPa at $R_{eff} = 0.46$ on the AB samples, then we could estimate a fatigue limit in the range of 190–210 MPa at $R_{eff} = -0.16$ for LSPed specimens, which is perfectly in line with experimental results.

This simple analysis clearly shows that, apart from modification of the internal cavities [36], the main effect of LSP is to induce compressive residual stresses able to significantly increase the fatigue strength [22,46].

Finally, some other aspects should be considered for a complete analysis of influencing factors: (i) the slight increase in hardness measured on all the investigated samples might produce limited modifications in fatigue strength; (ii) any possible relaxation of residual stresses and of the work-hardening condition might be expected over the fatigue lives of the samples. Both effects have been assumed to be negligible for the conditions investigated and have not been accounted for in the model.

5. Conclusions

The effects of LSP on different surface conditions (cubic specimens) of L-PBF AlSi7Mg were investigated considering samples fabricated with different laser process parameters for contour scanning, resulting in diverse surface profiles with different characteristics. The quality of the LSPed surfaces were investigated through multi-scale surface analysis utilizing SEM/EDS (general surface morphology and variation in the chemical composition of the surface as a result of LSP treatment), confocal microscopy (providing quantitative information on the surface features such as peaks and valleys), analysis of the polished cross-sections (allowing the observation of sub-surface and re-entrant features which are not possible to be observed through confocal microscopy) and hole drilling (measuring the residual stresses from the surface to 1 mm of depth in LSPed samples. The studied LSP condition was applied on the L-PBFed bending fatigue specimens and a qualitative correlation was found through micro-CT results of the fatigue specimens and the analysis of the cubic specimens. Moreover, EBSD analysis were performed on the LSPed fatigue specimens to evaluate the effect of LSP treatment on the texture evolution. The fracture surfaces were carefully investigated after performing bending fatigue tests on three sets of specimens. Furthermore, simple fracture mechanics analysis revealed the dominant effect of residual stresses on the fatigue life improvements in LSPed specimens.

Table 5
Comparison of fatigue limits and the corresponding effective stress ratios.

	LSP	AB
Fatigue limit stress range	200 [MPa]	130 [MPa]
Effective stress ratio (R_{eff})	−0.16	0.46

The following conclusions were drawn

- No significant changes in the surface roughness was observed after LSP, while the laser peening process induced a clear compressive residual stress profile throughout the sample;
- The closure of re-entrant features and sub-surface porosity was achieved after the LSP treatment, as confirmed through polished section and CT scan analysis;
- Laser peening resulted in microstructural changes down to 50 μm below the surface via plastic deformation, which led to a measurable change in grain shape (aspect ratio) and slight increase in microhardness in subsurface regions up to a depth of about 300 um;
- The fatigue strength of LSPed specimens improved substantially (by around 50% compared to AB specimens). Such increase can be attributed to the beneficial effect of compressive residual stresses.

Declaration of Competing Interest

The authors declare that they have no known competing financial interests or personal relationships that could have appeared to influence the work reported in this paper.

Data availability

Data will be made available on request.

Acknowledgements

The support by the Italian Ministry for Education, University and Research (MIUR) through the project headed "Department of Excellence LIS4.0" (Integrated Laboratory for Lightweight and Smart Structures) is acknowledged. Additional thanks to Dr. Charlotte de Formanoir for her assistance in the literature review process.

References

[1] T. DebRoy, H.L. Wei, J.S. Zuback, T. Mukherjee, J.W. Elmer, J.O. Milewski, A. M. Beese, A. Wilson-Heid, A. De, W. Zhang, Additive manufacturing of metallic components – process, structure and properties, Prog. Mater. Sci. 92 (2018) 112–224, https://doi.org/10.1016/j.pmatsci.2017.10.001.
[2] D. Herzog, V. Seyda, E. Wycisk, C. Emmelmann, Additive manufacturing of metals, Acta Mater. (2016), https://doi.org/10.1016/j.actamat.2016.07.019.

[3] D.D. Gu, W. Meiners, K. Wissenbach, R. Poprawe, Laser additive manufacturing of metallic components: materials, processes and mechanisms, Int. Mater. Rev. 57 (2012) 133–164, https://doi.org/10.1179/1743280411Y.0000000014.

[4] N. Sohrabi, J. Jhabvala, R.E. Logé, Additive manufacturing of bulk metallic glasses-process, challenges and properties: a review, Metals (Basel). 11 (2021) 1279, https://doi.org/10.3390/met11081279.

[5] M. Hamidi Nasab, M. Vedani, E. Boillat, R.E. Logé, A Study on the Surface Features of the SLM Processed Parts and Their Journey to Become Bulk Defects, in: Eur. Powder Metall. Assoc., 2019.

[6] J.-P. Kruth, J. Deckers, E. Yasa, R. Wauthlé, Assessing and comparing influencing factors of residual stresses in selective laser melting using a novel analysis method, Proc. Inst. Mech. Eng. Part B J. Eng. Manuf. 226 (2012) 980–991, https://doi.org/10.1177/0954405412437085.

[7] M. Hamidi Nasab, S. Romano, D. Gastaldi, S. Beretta, M. Vedani, Combined effect of surface anomalies and volumetric defects on fatigue assessment of AlSi7Mg fabricated via laser powder bed fusion, Addit. Manuf. 34 (2020), https://doi.org/10.1016/j.addma.2019.100918.

[8] N. Sohrabi, M. Hamidi-Nasab, B. Rouxel, J. Jhabvala, A. Parrilli, M. Vedani, R. E. Logé, Fatigue performance of an additively manufactured Zr-based bulk metallic glass and the effect of post-processing, Met. 11 (2021), https://doi.org/10.3390/met11071064.

[9] M. Hamidi Nasab, A. Giussani, D. Gastaldi, V. Tirelli, M. Vedani, Effect of surface and subsurface defects on fatigue behavior of AlSi10Mg alloy processed by laser powder bed fusion (L-PBF), Metals (Basel). 9 (2019) 1063, https://doi.org/10.3390/met9101063.

[10] M.H. Nasab, D. Gastaldi, N.F. Lecis, M. Vedani, On morphological surface features of the parts printed by selective laser melting (SLM), Addit. Manuf. 24 (2018) 373–377, https://doi.org/10.1016/j.addma.2018.10.011.

[11] U. Zerbst, G. Bruno, J.-Y. Buffière, T. Wegener, T. Niendorf, T. Wu, X. Zhang, N. Kashaev, G. Meneghetti, N. Hrabe, M. Madia, T. Werner, K. Hilgenberg, M. Koukolíková, R. Procházka, J. Džugan, B. Möller, S. Beretta, A. Evans, R. Wagener, K. Schnabel, Damage tolerant design of additively manufactured metallic components subjected to cyclic loading: state of the art and challenges, Prog. Mater. Sci. 121 (2021), 100786, https://doi.org/10.1016/j.pmatsci.2021.100786.

[12] A. du Plessis, S. Beretta, Killer notches: the effect of as-built surface roughness on fatigue failure in AlSi10Mg produced by laser powder bed fusion, Addit. Manuf. 35 (2020), 101424, https://doi.org/10.1016/j.addma.2020.101424.

[13] S. Beretta, M. Gargourimotlagh, S. Foletti, A. du Plessis, M. Riccio, Fatigue strength assessment of "as built" AlSi10Mg manufactured by SLM with different build orientations, Int. J. Fatigue 139 (2020), 105737, https://doi.org/10.1016/j.ijfatigue.2020.105737.

[14] M. Hamidi Nasab, A. Falzetti, A. Redaelli, N. Lecis, A. Giussani, L. Sala, M. Vedani, Finishing of internal and external surfaces produced by Powder Bed Fusion, in: SIG Addit. Manuf, 2017.

[15] E. Maleki, S. Bagherifard, S.M.J. Razavi, M. Riccio, M. Bandini, A. du Plessis, F. Berto, M. Guagliano, Fatigue behaviour of notched laser powder bed fusion AlSi10Mg after thermal and mechanical surface post-processing, Mater. Sci. Eng. A 829 (2022), 142145, https://doi.org/10.1016/j.msea.2021.142145.

[16] W.H. Kan, Y. Nadot, M. Foley, L. Ridosz, G. Proust, J.M. Cairney, Factors that affect the properties of additively-manufactured AlSi10Mg: porosity versus microstructure, Addit. Manuf. 29 (2019), 100805, https://doi.org/10.1016/j.addma.2019.100805.

[17] A. du Plessis, E. Macdonald, Hot isostatic pressing in metal additive manufacturing: X-ray tomography reveals details of pore closure, Addit. Manuf. 34 (2020), 101191, https://doi.org/10.1016/j.addma.2020.101191.

[18] S. Tammas-Williams, P.J. Withers, I. Todd, P.B. Prangnell, The effectiveness of hot isostatic pressing for closing porosity in titanium parts manufactured by selective Electron beam melting, Metall. Mater. Trans. A. 47 (2016) 1939–1946, https://doi.org/10.1007/s11661-016-3429-3.

[19] J.J. Lewandowski, M. Seifi, Metal additive manufacturing: a review of mechanical properties, Annu. Rev. Mater. Res. 46 (2016) 151–186.

[20] E. Maleki, S. Bagherifard, M. Bandini, M. Guagliano, Surface post-treatments for metal additive manufacturing: Progress, challenges, and opportunities, Addit. Manuf. 37 (2021), 101619, https://doi.org/10.1016/J.ADDMA.2020.101619.

[21] M. Hamidi Nasab, A. Giussani, D. Gastaldi, V. Tirelli, M. Vedani, Effect of surface and subsurface defects on fatigue behavior of AlSi10Mg alloy processed by laser powder bed fusion (L-PBF), Metals (Basel) 9 (2019) 1063, https://doi.org/10.3390/met9101063.

[22] M. Benedetti, E. Torresani, M. Leoni, V. Fontanari, M. Bandini, C. Pederzolli, C. Potrich, The effect of post-sintering treatments on the fatigue and biological behavior of Ti-6Al-4V ELI parts made by selective laser melting, J. Mech. Behav. Biomed. Mater. 71 (2017) 295–306, https://doi.org/10.1016/j.jmbbm.2017.03.024.

[23] L. Hackel, J.R. Rankin, A. Rubenchik, W.E. King, M. Matthews, Laser peening: a tool for additive manufacturing post-processing, Addit. Manuf. 24 (2018) 67–75, https://doi.org/10.1016/j.addma.2018.09.013.

[24] S. Luo, W. He, K. Chen, X. Nie, L. Zhou, Y. Li, Regain the fatigue strength of laser additive manufactured Ti alloy via laser shock peening, J. Alloys Compd. 750 (2018) 626–635, https://doi.org/10.1016/j.jallcom.2018.04.029.

[25] P. Yella, K.V. Rajulapati, G.V. Prasad Reddy, R. Sandhya, P. Prem Kiran, R. K. Buddu, K. Bhanu Sankara Rao, Effect of laser shock peening on high cycle fatigue characteristics of 316LN stainless steel, Int. J. Press. Vessel. Pip. 176 (2019), 103972, https://doi.org/10.1016/j.ijpvp.2019.103972.

[26] S. Huang, J. Zhao, J. Sheng, X. Meng, E. Agyenim-Boateng, D. Ma, J. Li, J. Zhou, Effect of laser peening with different power densities on vibration fatigue resistance of hydrogenated TC4 titanium alloy, Int. J. Fatigue 131 (2020), 105335, https://doi.org/10.1016/j.ijfatigue.2019.105335.

[27] K. Yang, Q. Huang, B. Zhong, Q. Wang, Q. Chen, Y. Chen, N. Su, H. Liu, Enhanced extra-long life fatigue resistance of a bimodal titanium alloy by laser shock peening, Int. J. Fatigue 141 (2020), 105868, https://doi.org/10.1016/j.ijfatigue.2020.105868.

[28] M. Kemal Kulekci, U. Esme, Critical analysis of processes and apparatus for industrial surface peening technologies, Int. J. Adv. Manuf. Technol. 74 (2014) 1551–1565, https://doi.org/10.1007/s00170-014-6088-9.

[29] N.E. Uzan, S. Ramati, R. Shneck, N. Frage, O. Yeheskel, On the effect of shot-peening on fatigue resistance of AlSi10Mg specimens fabricated by additive manufacturing using selective laser melting (AM-SLM), Addit. Manuf. 21 (2018) 458–464, https://doi.org/10.1016/J.ADDMA.2018.03.030.

[30] J. Damon, S. Dietrich, F. Vollert, J. Gibmeier, V. Schulze, Process dependent porosity and the influence of shot peening on porosity morphology regarding selective laser melted AlSi10Mg parts, Addit. Manuf. 20 (2018) 77–89, https://doi.org/10.1016/J.ADDMA.2018.01.001.

[31] D.J. Chadwick, S. Ghanbari, D.F. Bahr, M.D. Sangid, C.D. Michael Sangid, Crack incubation in shot peened AA7050 and mechanism for fatigue enhancement, Fatigue Fract. Eng. Mater. Struct. 41 (2018) 71–83, https://doi.org/10.1111/ffe.12652.

[32] M. Munther, T. Martin, A. Tajyar, L. Hackel, A. Beheshti, K. Davami, Laser shock peening and its effects on microstructure and properties of additively manufactured metal alloys: a review, Eng. Res. Express. 2 (2020) 22001, https://doi.org/10.1088/2631-8695/ab9b16.

[33] N. Kalentics, E. Boillat, P. Peyre, S. Ćirić-Kostić, N. Bogojević, R.E. Logé, Tailoring residual stress profile of selective laser melted parts by laser shock peening, Addit. Manuf. (2017), https://doi.org/10.1016/j.addma.2017.05.008.

[34] E. Maleki, S. Bagherifard, O. Unal, M. Bandini, M. Guagliano, On the effects of laser shock peening on fatigue behavior of V-notched AlSi10Mg manufactured by laser powder bed fusion, Int. J. Fatigue 163 (2022), 107035, https://doi.org/10.1016/j.ijfatigue.2022.107035.

[35] N. Kalentics, M.O.V. de Seijas, S. Griffiths, C. Leinenbach, R.E. Logé, 3D laser shock peening – a new method for improving fatigue properties of selective laser melted parts, Addit. Manuf. 33 (2020), 101112, https://doi.org/10.1016/j.addma.2020.101112.

[36] Q. Jiang, S. Li, C. Zhou, B. Zhang, Y. Zhang, Effects of laser shock peening on the ultra-high cycle fatigue performance of additively manufactured Ti6Al4V alloy, Opt. Laser Technol. 144 (2021), 107391, https://doi.org/10.1016/j.optlastec.2021.107391.

[37] Y. Jing, X. Fang, N. Xi, X. Feng, K. Huang, Investigation of microstructure and mechanical properties evolution in 7050 aluminum alloy and 316L stainless steel treated by laser shock peening, Mater. Charact. 182 (2021), 111571, https://doi.org/10.1016/j.matchar.2021.111571.

[38] J. Lu, H. Lu, X. Xu, J. Yao, J. Cai, K. Luo, High-performance integrated additive manufacturing with laser shock peening –induced microstructural evolution and improvement in mechanical properties of Ti6Al4V alloy components, Int. J. Mach. Tools Manuf. 148 (2020), 103475, https://doi.org/10.1016/j.ijmachtools.2019.103475.

[39] N. Kalentics, A. Burn, M. Cloots, R.E. Logé, 3D laser shock peening as a way to improve geometrical accuracy in selective laser melting, Int. J. Adv. Manuf. Technol. 101 (2019) 1247–1254, https://doi.org/10.1007/s00170-018-3033-3.

[40] W. Guo, R. Sun, B. Song, Y. Zhu, F. Li, Z. Che, B. Li, C. Guo, L. Liu, P. Peng, Laser shock peening of laser additive manufactured Ti6Al4V titanium alloy, Surf. Coat. Technol. 349 (2018) 503–510, https://doi.org/10.1016/j.surfcoat.2018.06.020.

[41] L. Chen, P. Gu, T. Ge, Y. Sun, L. Li, X. Ren, Effect of laser shock peening on microstructure and mechanical properties of TiC strengthened inconel 625 alloy processed by selective laser melting, Mater. Sci. Eng. A 835 (2022), 142610, https://doi.org/10.1016/j.msea.2022.142610.

[42] C. Wang, L. Wang, C.-L. Wang, K. Li, X.-G. Wang, Dislocation density-based study of grain refinement induced by laser shock peening, Opt. Laser Technol. 121 (2020), 105827, https://doi.org/10.1016/j.optlastec.2019.105827.

[43] R. Sun, L. Li, Y. Zhu, W. Guo, P. Peng, B. Cong, J. Sun, Z. Che, B. Li, C. Guo, L. Liu, Microstructure, residual stress and tensile properties control of wire-arc additive manufactured 2319 aluminum alloy with laser shock peening, J. Alloys Compd. 747 (2018) 255–265, https://doi.org/10.1016/j.jallcom.2018.02.353.

[44] H. Zhang, Z. Cai, J. Chi, G. Han, R. Sun, Z. Che, H. Zhang, W. Guo, Microstructural evolution, mechanical behaviors and strengthening mechanism of 300 M steel subjected to multi-pass laser shock peening, Opt. Laser Technol. 148 (2022), 107726, https://doi.org/10.1016/j.optlastec.2021.107726.

[45] L. Lan, X. Jin, S. Gao, B. He, Y. Rong, Microstructural evolution and stress state related to mechanical properties of electron beam melted Ti-6Al-4V alloy modified by laser shock peening, J. Mater. Sci. Technol. 50 (2020) 153–161, https://doi.org/10.1016/j.jmst.2019.11.039.

[46] N. Kalentics, K. Huang, M. Ortega Varela de Seijas, A. Burn, V. Romano, R.E. Logé, Laser shock peening: a promising tool for tailoring metallic microstructures in selective laser melting, J. Mater. Process. Technol. 266 (2019) 612–618, https://doi.org/10.1016/j.jmatprotec.2018.11.024.

[47] M. Morgano, N. Kalentics, C. Carminati, J. Capek, M. Makowska, R. Woracek, T. Maimaitiyili, T. Shinohara, R. Loge, M. Strobl, Investigation of the effect of laser shock peening in additively manufactured samples through Bragg edge neutron imaging, Addit. Manuf. 34 (2020), 101201, https://doi.org/10.1016/j.addma.2020.101201.

[48] A. du Plessis, D. Glaser, H. Moller, N. Mathe, L. Tshabalala, B. Mfusi, R. Mostert, Pore closure effect of laser shock peening of additively manufactured AlSi10Mg, 3D print, Addit. Manuf. 6 (2019) 245–252, https://doi.org/10.1089/3dp.2019.0064.

[49] P. Yella, K.V. Rajulapati, G.V. Prasad Reddy, R. Sandhya, P. Prem Kiran, R. K. Buddu, K. Bhanu Sankara Rao, Effect of laser shock peening on high cycle fatigue characteristics of 316LN stainless steel, Int. J. Press. Vessel. Pip. 176 (2019), 103972, https://doi.org/10.1016/j.ijpvp.2019.103972.
[50] S. Huang, J. Zhao, J. Sheng, X. Meng, E. Agyenim-Boateng, D. Ma, J. Li, J. Zhou, Effect of laser peening with different power densities on vibration fatigue resistance of hydrogenated TC4 titanium alloy, Int. J. Fatigue 131 (2020), 105335, https://doi.org/10.1016/j.ijfatigue.2019.105335.
[51] K. Yang, Q. Huang, B. Zhong, Q. Wang, Q. Chen, Y. Chen, N. Su, H. Liu, Enhanced extra-long life fatigue resistance of a bimodal titanium alloy by laser shock peening, Int. J. Fatigue 141 (2020), 105868, https://doi.org/10.1016/j.ijfatigue.2020.105868.
[52] Z. Qin, B. Li, X. Huang, H. Zhang, R. Chen, M. Adeel, H. Xue, The effect of laser shock peening on surface integrity and high and very high cycle fatigue properties of 2024-T351 aluminum alloy, Opt. Laser Technol. 149 (2022), 107897, https://doi.org/10.1016/j.optlastec.2022.107897.
[53] D. Courapied, L. Berthe, P. Peyre, F. Coste, J.-P. Zou, A.-M. Sautivet, Laser-delayed double shock-wave generation in water-confinement regime, J. Laser Appl. (2015), https://doi.org/10.2351/1.4906382.
[54] N.J. Rendler, I. Vigness, Hole-drilling strain-gage method of measuring residual stresses, Exp. Mech. 6 (1966) 577–586, https://doi.org/10.1007/BF02326825.
[55] ASTM International, ASTM E837–20: Standard Test Method for Determining Residual Stresses by the Hole-Drilling Strain-Gage Method, 2021.
[56] A. Thompson, N. Senin, I. Maskery, L. Körner, S. Lawes, R. Leach, Internal surface measurement of metal powder bed fusion parts, Addit. Manuf. 20 (2018) 126–133, https://doi.org/10.1016/j.addma.2018.01.003.
[57] International Organization for Standardization, ISO 25178-2, Geometrical Product Specifications (GPS) - Surface Texture: Areal Part 2: Terms, Definitions and Surface Texture Parameters, 2007.
[58] G.T. Smith, Machined surface integrity, in: G.T. Smith (Ed.), Ind. Metrol. Surfaces Roundness, Springer, London, London, 2002, pp. 185–247, https://doi.org/10.1007/978-1-4471-3814-3_5.
[59] L. Boniotti, S. Beretta, L. Patriarca, L. Rigoni, S. Foletti, Experimental and numerical investigation on compressive fatigue strength of lattice structures of AlSi7Mg manufactured by SLM, Int. J. Fatigue (2019), https://doi.org/10.1016/j.ijfatigue.2019.06.041.
[60] R. Casati, M. Vedani, Aging response of an A357 Al alloy processed by selective laser melting, Adv. Eng. Mater. 0 (2018), https://doi.org/10.1002/adem.201800406, 1800406.
[61] A. du Plessis, S.G. le Roux, A. Guelpa, The CT scanner Facility at Stellenbosch University: an open access X-ray computed tomography laboratory, Nucl. Instruments Methods Phys. Res. Sect. B Beam Interact. Mater. Atoms. 384 (2016) 42–49, https://doi.org/10.1016/j.nimb.2016.08.005.
[62] A. Townsend, L. Pagani, P.J. Scott, L. Blunt, Introduction of a surface characterization parameter Sdr prime for analysis of re-entrant features, J. Nondestruct. Eval. (2019), https://doi.org/10.1007/s10921-019-0573-x.
[63] N.C. Levkulich, S.L. Semiatin, J.E. Gockel, J.R. Middendorf, A.T. DeWald, N. W. Klingbeil, The effect of process parameters on residual stress evolution and distortion in the laser powder bed fusion of Ti-6Al-4V, Addit. Manuf. 28 (2019) 475–484, https://doi.org/10.1016/j.addma.2019.05.015.
[64] Y. Liu, S. Mahadevan, Probabilistic fatigue life prediction using an equivalent initial flaw size distribution, Int. J. Fatigue 31 (2009) 476–487, https://doi.org/10.1016/j.ijfatigue.2008.06.005.
[65] M.H. El Haddad, K.N. Smith, T.H. Topper, Fatigue crack propagation of short cracks, J. Eng. Mater. Technol. 101 (1979) 42–46, https://doi.org/10.1115/1.3443647.
[66] Murakami Beretta, SIF and threshold for small cracks at small notches under torsion, Fatigue Fract. Eng. Mater. Struct. 23 (2000) 97–104, https://doi.org/10.1046/j.1460-2695.2000.00260.x.
[67] Y. Murakami, Chapter 2 - stress concentration, in: Y.B.T.-M.F. Murakami (Ed.), Met. Fatigue, Elsevier Science Ltd, Oxford, 2002, pp. 11–24, https://doi.org/10.1016/B978-008044064-4/50002-5.
[68] K.J. Miller, The short crack problem, Fatigue Fract. Eng. Mater. Struct. (1982), https://doi.org/10.1111/j.1460-2695.1982.tb01250.x.